Building and Environment 252 (2024) 111290

Contents lists available at ScienceDirect

Building and Environment

journal homepage: www.elsevier.com/locate/buildenv

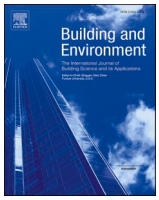

Investigation on the thermal budget and flow field of a manikin and comparison with human subject in different scenarios

Abhilash Sankaran [a,*], Rainer Hain [a], Christina Matheis [b], Thomas Fuchs [a], Victor Norrefeldt [b], Gunnar Grün [b,c], Christian J. Kähler [a]

[a] University of the Bundeswehr Munich, Institute of Fluid Mechanics and Aerodynamics, 85577, Neubiberg, Germany
[b] Fraunhofer Institute for Building Physics IBP, 83626, Valley, Germany
[c] University of Stuttgart, Institute for Acoustics and Building Physics, 70569, Stuttgart, Germany

A B S T R A C T

The thermal plume from a human significantly influences indoor air flows, impacting the dispersion of air constituents and consequently affecting indoor air quality. This is also relevant in the transport of respiratory particles, which results in spread of respiratory diseases including COVID-19 caused by SARS-CoV-2. Our focus is on the sitting condition, a common scenario in various ventilated spaces. Prior human thermal plume studies employed predominantly anemometers to measure flow field which lack spatial resolution and detailed flow field. Here, Particle Image Velocimetry (PIV) is utilized to directly visualize and analyze the human thermal plume. No direct comparison of thermal manikin and real human subject is considered in previous studies. Such experiments were performed with a thermal manikin and comparisons were made with a real human. The results show that the thermal plume from manikin without breathing function and the real person have similarities including bi-lobe structure of the flow field. The integral fluxes like volumetric flux, momentum flux, buoyancy force flux, and enthalpy flux were determined and compared. The average volume flux of real person and the thermal manikin was found to be 153 m^3/h and 125 m^3/h, respectively. The momentum flux was 0.005 N for both the cases. The estimation of enthalpy flux revealed that radiative heat transfer dominates and less than 50 % of the total flux is convected in the human thermal plume. In addition, a zonal simulation model was created and the volumetric flux was determined by simulation and is compared to the measured values.

1. Introduction

A human thermal plume induces a considerable flow in indoor conditions. This leads to the importance of human thermal plumes to the flow behavior in rooms [1]. Such flows are important in designing different indoor ventilation systems like mixing and displacement ventilation. In case of displacement ventilation, it is important to know the volumetric flow contribution from humans as that adds to the driving of the flow to the ventilation system [2]. In case of mixing ventilation, human thermal plumes add primarily to the mixing of the clean and polluted air [3,4]. For both the systems, it is important to have both qualitative and quantitative understanding of the contribution from the thermal plume of a human body. In case of mixing ventilation, human thermal plumes could impede the flow of fresh air towards the breathing zone, while the added turbulent intensity could aid diluting the concentration of the aerosol containing microbes or pollutants in air [3,4]. For displacement ventilation, the mean flow of thermal plume itself contributes for the bulk transport of the ventilation flow. However, induced mixing is generally not desirable in the lower regions, where occupants are present, as mixing results in transport of pollutants in the area, which is expected to be clean [5]. Here, the goal is to understand the induced flow due to human thermal plume without the effect of the external ventilation flows. This aids in specifically understanding the contribution of the human factor alone and serves as a foundation for simulating scenarios with manikins. The focus is on a sitting position, a prevalent scenario in numerous ventilated spaces such as offices, classrooms, and theaters, among others.

The human thermal plume influences the airflow in human microenvironments and hence dispersion of air constituents to and from the breathing zone [3,6,7]. This is also relevant for the transport of respiratory particles. These may contain viruses like the influenza virus or SARS-CoV-2. Hence, this has renewed the interest in understanding the influence of human thermal plume in the micro-environment and inhalation exposure [3,7,8]. The expired flow from breathing is also influenced by the rising thermal plume affecting their trajectory and carried up along with the plume. A numerical study [9] has shown that initial high velocity cough flow could also be ascended by the thermal plume of the body. Understanding the overall flow behavior is important

* Corresponding author.
E-mail address: abhilash.sankaran@unibw.de (A. Sankaran).

https://doi.org/10.1016/j.buildenv.2024.111290
Received 9 October 2023; Received in revised form 19 January 2024; Accepted 8 February 2024
Available online 9 February 2024

for designing solutions like physical barriers or air curtains [6] to improve the delivery of clean air to the occupants. The thermal plume is also important for special indoor environments like surgery rooms and clean rooms [10]. Humans emit volatile organic compounds (VOCs) and exfoliated skin, which is again carried by the human thermal plume [10,11]. The measurement of chemical signals in the human thermal plume is a potential sampling method for purposes including medical diagnosis or detection of concealed explosive trace [10–12].

Some studies have been conducted on thermal manikin flows and the effect of different parameters like clothing, breathing, and body posture [13–15]. Thermal plumes above male human subjects were carried out in Ref. [16]. Most of the studies relied on multiple anemometers capable of measuring only absolute velocities above 0.05 m/s [13–17]. The review [18] discusses the importance of PIV measurements for indoor flows, which give detailed information on the complex flow fields including instantaneous velocity fields in addition to turbulent properties. However, studies on high resolution flow field measurements of the human thermal plume are rare. Previous PIV studies on manikin involve the effect of standing and sitting [1], breathing zone flow [19], and effect of confinement [20]. A planar PIV measurement of a standing human male was also conducted in Ref. [8]. However, specifically the eddy convective-velocity field was measured due to large field of view measurement as individual particles were not resolvable [8]. This could lead to erroneous velocities when out-of-field motions are present.

Further, understanding of the overall thermal budget of humans in indoor condition is useful to predict and simulate the effective induced flow and the micro-environment around the human. In scenarios involving expansive spaces such as substantial rooms or buildings, a pragmatic method for approximating these combined effects involves the adoption of a zonal-based approach [21,22]. This strategy proves advantageous particularly in situations where employing Computational Fluid Dynamics (CFD) would prove excessively time-consuming for simulations like three dimensional rooms. The zonal-based approach offers a practical means of ascertaining overall heat transfer and total fluid flow within large indoor conditions.

As mentioned above, only few of the studies involved real human subjects. Further, there has been no direct comparison of thermal manikin and human thermal plume. In this regard, the main contributions of the article include.

- Complete description of the velocity field of human thermal plume including the rising breath revealing the bi-lobe structure in average field.
- Direct comparison of the plume from the manikin without breathing function to a real human subject and comparison between different scenarios with human subject.
- Instantaneous flow field above the head with all flow components resulting in comparison of the modes in the fluctuating field.
- The thermal budget of the thermal manikin with consideration of the split between the radiative and convective heat transfer.
- Comparison of the volumetric flux by measurements and a zonal simulation approach.

2. Experiments

2.1. Setup and procedure

The measurements were carried out in a room with a size of 2.8 m^L × 2.5 m^W × 2.5 m^H. This small room was realized by a housing within a larger room, keeping thermal effects through the walls as small as possible. The schematic of the stereoscopic PIV experimental setup is shown in Fig. 1. The housing has openings for camera view and the laser light-sheet. The measurement equipment including the two cameras, the laser, and the computers was placed outside the housing. Due to the large field of view, an in-house built calibration target based on LEGO was utilized [23]. The thermal manikin (average power approximately

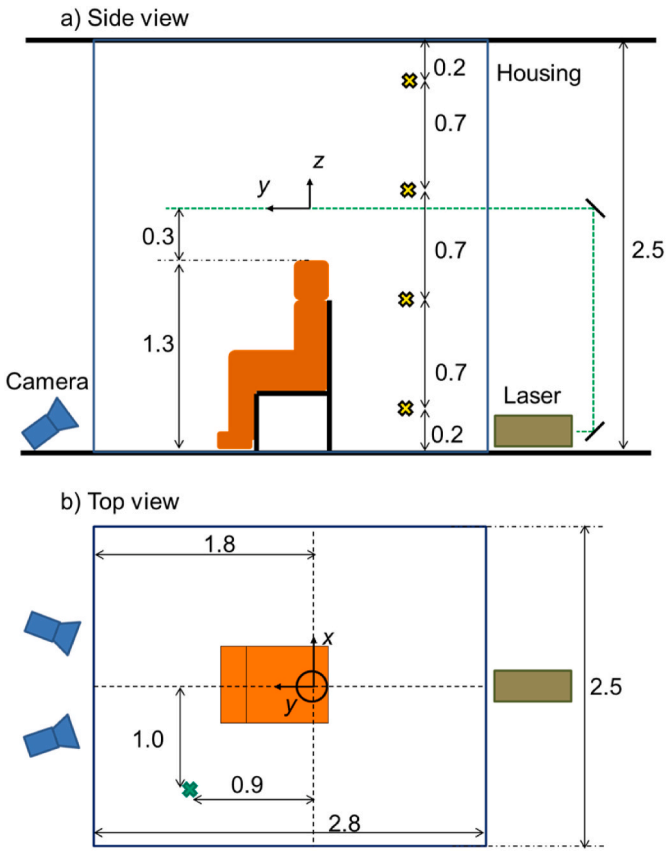

Fig. 1. (A) Experimental setup for stereoscopic PIV, yellow × sign indicates the temperature sensor position to measure the room temperature gradient. (b) The top view within the housing enclosing the manikin, green × sign indicates the temperature sensor position to measure room temperature at the laser height for thermal field determination. (For interpretation of the references to color in this figure legend, the reader is referred to the Web version of this article.)

80 W) was switched on 1 hour prior to the start of the experiments and the room was nebulized by DEHS particles with a mean diameter of $d_p \approx$ 0.4 μm. The thermal manikin does not have a breathing function and incorporates only thermal convection boundary layer. The measurement plane was located 30 cm above the head of the manikin. The images were recorded with two Imager sCMOS cameras from LaVision GmbH (Germany) using Zeiss Makro Planar 50 mm lenses. 2000 image pairs were recorded at an image pair acquisition rate of 1 Hz. Further tests were also conducted with a real person and comparisons are made. The measuring system was controlled by the DaVis 10 software from LaVision GmbH, which was also utilized for data evaluation.

The interest in this work is to study the effect of human in a room where the wall effects could be considered negligible. Initial experiments, outlined in the supplementary information, revealed challenges in controlling large-scale flows within the large room, leading to significant wandering of the thermal plume. Capturing the entire plume under these conditions proved to be challenging. Consequently, we choose a smaller room that still maintains sufficient size to disregard wall effects. The chosen area, 7.5 m^2, is smaller than an individual office space and is more characteristic of an open plan or workstation space [24]. This is deemed adequate for examining the contribution of a person's flow, with the exception of large scale flows inherent to large rooms. This adjustment ensures a more manageable experimental setup.

The control mechanism of the heat input to the manikin is important. Some studies consider a constant outer skin temperature for the manikin, while others define a fixed heat input to the manikin. The response of the manikin would be different according to the control mechanism chosen. Here, we consider a constant heat input to the

manikin. The assumption in this case is that individuals indoors are attired in appropriate clothing to facilitate comfortable heat dissipation from the body.

One of the challenges in large area PIV visualization in air is to find the optimum between enough scattered light from particles, which are still reliable tracers [18]. Larger particles would lead to more scattered light; however, it must be ensured that they sufficiently follow the flow. One of the methods to satisfy the above conditions is to utilize helium-filled soap bubbles (diameter of few hundred micrometers) [25]. However, the lifetime of such bubbles is small (~5 min) which might not be enough for equilibration and to acquire statistical data. Therefore, the Stokes number and the sedimentation velocity due to gravity have to be considered. The Stokes number is defined by $St = \tau_p u_0 / l_0$ [26], with u_0 being the characteristic flow velocity, l_0 the characteristic length scale, and τ_p the particle relaxation time. DEHS particles with an average diameter of 0.4 μm in air lead to a particle relaxation time of $\tau_p \approx 4 \cdot 10^{-7}$ s [27]. Considering the order of magnitude of the velocity, (10^{-1} m/s), and the length scale (10^{-2} m) (resolution of the PIV measurements), the calculated Stokes number is $St \approx \mathcal{O}(10^{-6})$, which is $\ll 1$ meaning that the particles follow the flow quite well. The sedimentation velocity u_g due to gravity can be determined by $u_g = d_p^2(\rho_p - \rho_f)g/(18\mu)$ [18], which leads to $u_g \approx 4$ μm/s. This is negligible compared to the flow velocity induced by the manikin and the human. Hence, the particles considered are reliable tracers.

To have enough scattered light from these small particles in a large area PIV visualization, the forward scattering mode was used. The laser is placed behind the thermal manikin, while the cameras are placed in the front (as shown in Fig. 1) ensuring high light intensities reaching the cameras.

The real person was male with a height of 1.8 m and a weight of 75 kg. The person was wearing formal dress with no coat on. Different scenarios of the real person were recorded: normal breathing via nose, talking, breathing with mask on, and normal breathing with person performing various actions. For these cases, 1000 image pairs were recorded.

Temperature measurements were carried out by PT100 sensors with an accuracy of ±0.03 °C (1/10 DIN accuracy) and the PT-104 data logger from Pico Technology. The vertical room temperature gradient was measured at the four locations as shown in Fig. 1a. For the measurements of the temperature field above the thermal manikin, three sensors scanned the area of interest with measurement time of 15 min at each location. The grid for these measurements is 4 cm × 4 cm. The average of these data of the last 7.5 min is considered for each location. This is to mitigate the effect of initial transience due to the movement of the sensors. Further, the excess temperature (ΔT) with respect to the room temperature at the same height (shown in Fig. 1b) is calculated.

2.2. Uncertainty analysis

Particle Image Velocimetry (PIV) analysis inherently involves random and systematic errors; however, quantification is a complex task. Nonetheless, obtaining an estimate for the uncertainty associated with PIV results is a valuable and essential practice.

One of the systematic errors likely to affect large field of view PIV measurements is peak locking [26]. This is the bias of the observed displacement towards integer values when the particle image diameter is smaller than ~2 pixels. The observed displacements in the stereoscopic results did not reveal any such bias. Further analysis was done on the two-dimensional PIV results from the cameras. The observed distributions of the x and y displacements are shown in Fig. 2a and b, respectively. The histograms reveal a mild peak locking with shoulder near the integral pixel values. Hence, the associated error is assumed to be small.

Further, the uncertainty of the measured stereoscopic instantaneous velocity was calculated with the uncertainty estimation implemented in DaVis [28] to be $V_u \sim 0.01$ m/s. The statistical error associated with the mean field could be estimated to be $V_u/\sqrt{N}$, where N is the total number of samples/snapshots analyzed. For the current case with $N = 1000$, the random error ~0.0003 m/s is very small.

3. Numerical simulations

For the numerical simulations, a zonal simulation model is created from the test setup. The model is based on the Velocity Propagation Zonal Model (VEPZO) [22] implemented in Modelica [29]. The zonal approach makes it possible to obtain locally resolved temperature distributions with small computational effort at reasonable accuracy and to predict flow patterns due to heat loads or mechanical air flows. An included radiant model calculates the long-wave radiant heat exchange between the surfaces contained in the model. Here, each surface has a thermal node with corresponding surface properties. The radiative exchange is calculated using a view factor matrix. The measurements described above serve as a basis of comparison.

In the simulations, the buoyancy plumes resulting from convective heat input by humans are investigated and these are compared with the measurements. The buoyancy volume flow, which is determined from the measured flow velocities perpendicular to the z-plane (see Fig. 3), is used as a comparison value. Furthermore, conclusions can be drawn about the enthalpy flow by recording and calculating the temperature difference due to the heat input.

For zonal modeling, the air volume in the experimental room is divided into 7 zones in the x-direction, 5 zones in the y-direction, and 6 zones in the z-direction. Fig. 3 shows the zonal grid of the simulation model and Table 1 lists the dimensions of each zone.

In addition, another simulation model with a finer zone grid in the considered area is created to investigate the dependence of the zone

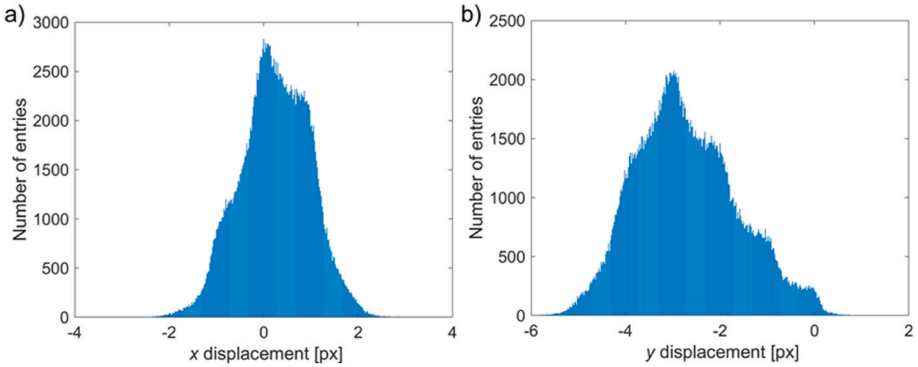

Fig. 2. Histogram of the (a) x and (b) y displacements in the 2D PIV analysis of the observed field.

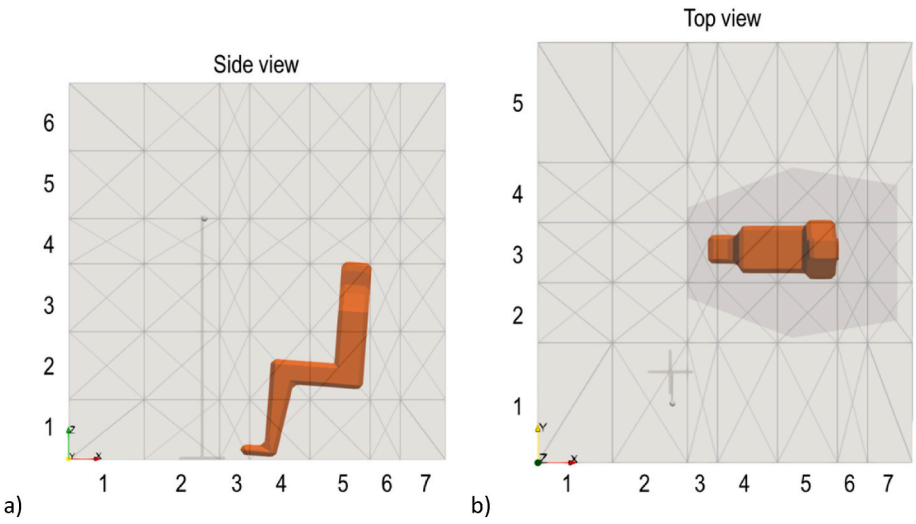

Fig. 3. Zoning of the test environment with position of the thermal manikin and a temperature sensor (a) in the *x*-*z* plane and (b) in the *x*-*y* plane with the 2 viewing planes in gray.

Table 1
Dimensions of the zonal model.

Zone-number	*x*-direction [m]	*y*-direction [m]	*z*-direction [m]
1	0.50	0.80	0.40
2	0.50	0.40	0.45
3	0.20	0.40	0.45
4	0.40	0.40	0.30
5	0.40	0.80	0.45
6	0.20		0.45
7	0.30		

sizes as well. The zone sizes and the details are presented in the supplementary information.

There are no ventilation sources or sinks in the model. The air flow results exclusively from the thermal conditions. For this purpose, a temperature of 24.3 °C is initialized as in the measurements. The bottom is assumed to be adiabatic, and the other enclosing surfaces are considered isothermal. In order to realistically represent the heat loads due to the manikin, it is implemented in the zonal model in different ways (see Fig. 4). The heat load in both variants is 80 W like in the experiment. The emitted heat load represents a defined heat source in the center of the respective zone. For the heat source, a convective as well as the radiative heat emission is taken into account.

In the finer model, the human heat load is divided into 22 zones. The division is done in the same way as in the model with the partitioned heat load by zones.

Because the model calculates the averaged flow velocities over a zone area, the simulated and measured velocities cannot be compared directly. The volume flows, instead, can be summed up over the considered area and thus form the basis for comparison between measurement and model. In the model, no distinction regarding heat loads is made between breathing and speaking, and wearing a mask. For the comparison the total head load of 80 W is considered. In addition, the excess temperature (ΔT) with respect to the room temperature is compared with the experimental data. The average temperatures of the last 7 min are used for comparison with the experiments.

4. Results

This section presents the average flow fields, fluctuating flow fields, integral properties obtained from experiments, and the simulation results from the zonal model.

4.1. Average velocity fields from experiments

Fig. 5 shows the mean velocity fields induced by the thermal manikin

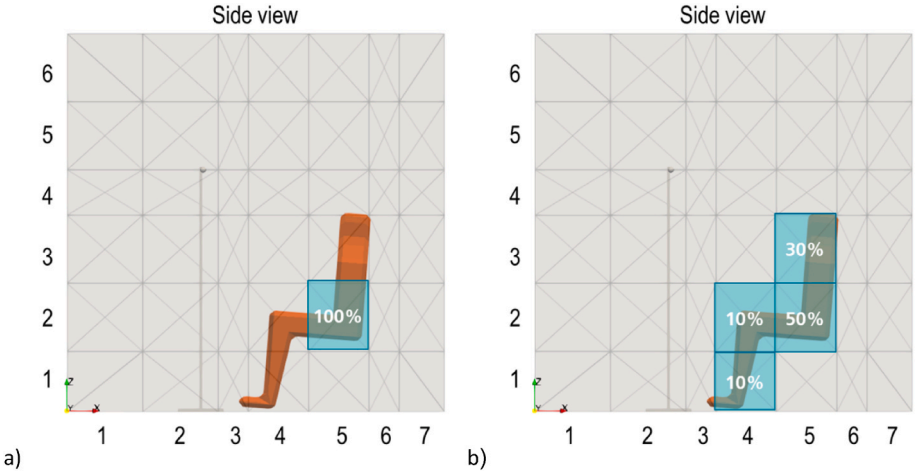

Fig. 4. Implementation of the human heat load in the model (a) by a central heat load or (b) by a zone partitioned heat load.

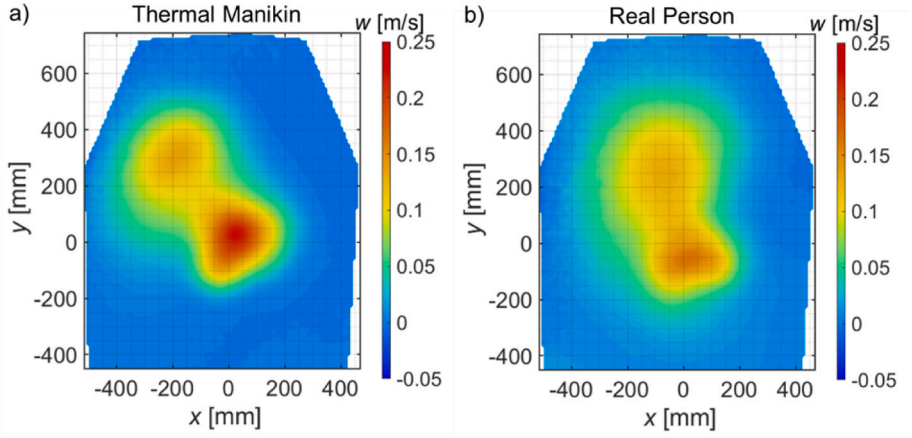

Fig. 5. Comparison of the *w*-component of the velocity contour above (a) the thermal manikin and (b) the real person. Average room temperature is 24.3 °C and 25.9 °C for thermal manikin and real person, respectively. Average vertical temperature gradient in the room is 0.34 K/m and 0.22 K/m for thermal manikin and real person, respectively. $x = 0$, $y = 0$ is directly above the center of the head.

and the real person. The results are obtained from 2000 statistically independent vector fields for the thermal manikin and 1000 statistically independent vector fields for the real person. In both cases, the recording was performed with 1 Hz acquisition rate. The center of the head is located at $x = 0, y = 0$. The field from the thermal manikin shows a more distinct lobe towards the front (off-centered to the left) with a second maximum of the vertical velocity. This results from the plume of the legs. For the real person with normal breathing (Fig. 5b), the plume reveals a qualitatively similar behavior with a clear lobe towards front. However, the peak of the vertical velocity component is lower (0.17 m/s) in case of the real person compared to the thermal manikin (0.23 m/s).

The plume axis meanders (or wanders) in time resulting in non-axisymmetric flow above the head in both the cases. Such wandering has been reported before with low temperature plumes including human thermal plumes [16]. The time dependent meandering was reduced with the incorporation of the housing, however it does not eliminate it.

Fig. 6 compares the flow fields for different scenarios with the real person: talking, and breathing with mask on. The comparison of the talking case (Fig. 6a) with the normal breathing case (Fig. 5b) reveals that the plume above the head is similar. However, when the person is talking, the second lobe is elongated further towards the front. This indicates the effect of the further propagation of the breath while speaking. On the other hand, when the person is wearing a mask (Fig. 6b), the second lobe is further constricted and nearly merges with the plume above the head. The peak of the vertical velocity component is lower (0.16 m/s) for the talking case compared to normal breathing (0.17 m/s), while it is slightly higher in case of wearing a mask (0.18 m/s).

Further, it is of interest to know how the thermal plume is modified by the person performing some actions – like normal movements of a person at a desk or cashier etc. A case with the person performing movements of such kind was conducted and the result is presented in Fig. 6c. The peak velocity is found to be 0.11 m/s which is significantly smaller in comparison to the other cases with the real person. However, the horizontal spread of the vertical velocity has increased. It can also been seen that the velocity does not approach zero towards the front indicating the extent of the plume to be larger than the visualized area. Further, some additional care has been taken in processing the raw data as the action sometimes lead to the person interfering the camera view, and these cases were not considered for the averaging shown here.

4.2. *Fluctuating velocity and Proper Orthogonal Decomposition (POD) analysis*

Fig. 7 reveals the standard deviation of the *w*-velocity component for the thermal manikin and the real person (with nasal breathing). It can be observed that the velocity field is completely captured as the standard deviation approaches zero within the visualization window.

For a more detailed analysis of the dynamics of the flow field, the instantaneous fluctuating velocity field is decomposed into a spatial part, the orthonormal bases $\varphi_n(x, y)$, and a temporal part with the coefficients $a_n^i(t)$ [20,30]:

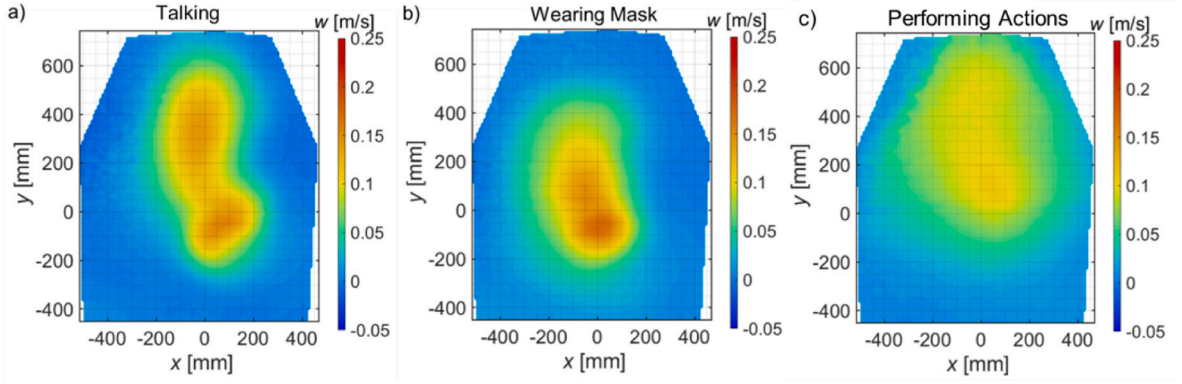

Fig. 6. Contour map of the *w*-velocity component of the velocity above the real person for scenarios: (a) talking, (b) wearing mask, and (c) performing actions. $x = 0$, $y = 0$ is directly above the center of the head. The average vertical temperature gradient in the room is 0.22 K/m with a room temperature of 25.9 °C.

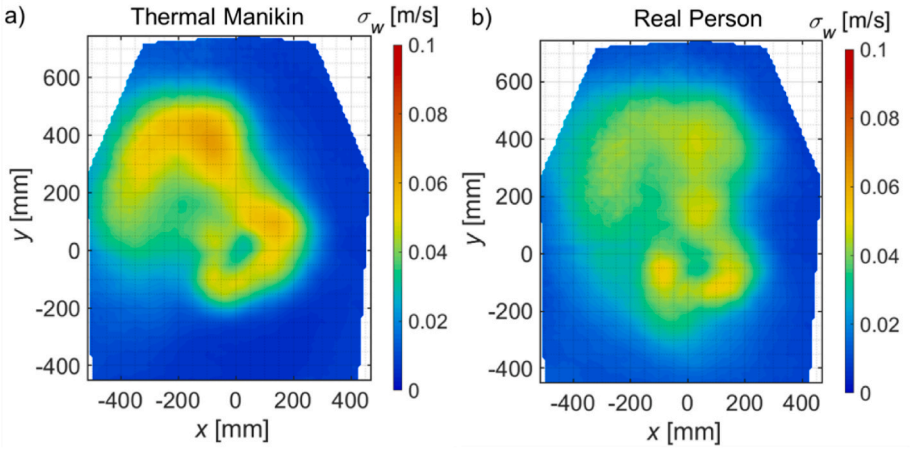

Fig. 7. Contour map of the standard deviation of the *w*-velocity component for (a) the thermal manikin and (b) the real person (nasal breathing). Average room temperature is 24.3 °C and 25.9 °C for the thermal manikin and the real person, respectively. The average vertical temperature gradient in the room is 0.34 K/m and 0.22 K/m for the thermal manikin and the real person, respectively. $x = 0$, $y = 0$ is directly above the center of the head.

$$u_i(x,y,t) = \sum_{n=0}^{N} a_n^i(t)\varphi_n(x,y) \tag{1}$$

where i represents the snapshot of an instantaneous velocity field and n the POD mode. Here, 1000 snapshots of the visualized flow in all the cases are analyzed. The eigenvalue λ_n of each mode φ_n characterizes the kinetic energy contained in the mode n, which is arranged in decreasing contribution of the kinetic energy.

The energy distribution between the modes of the thermal manikin and the real person is presented in Fig. 8a. Further, the comparison of the real person cases of normal breathing, with mask and talking also resulted in energy distributions which nearly overlap (not shown here). The first 20 to 30 modes account for approx. 50 % of the total energy and a few hundred modes for 80 % of the total energy. This indicates that the energy is distributed in a significant high number of modes and cannot be simplified considering only a few modes. It is interesting that the distribution of the thermal manikin flow is similar to the real person though thermal manikin does not incorporate breathing (see Fig. 8a).

Further analysis was conducted with merging all cases: thermal manikin, real person cases of normal breathing, with mask and talking. Fig. 8b demonstrates the energy distribution among the modes, which reveals a similar pattern to Fig. 8a. This indicates that all the cases share many of the modes. Fig. 8c displays the physical modes of the ensemble

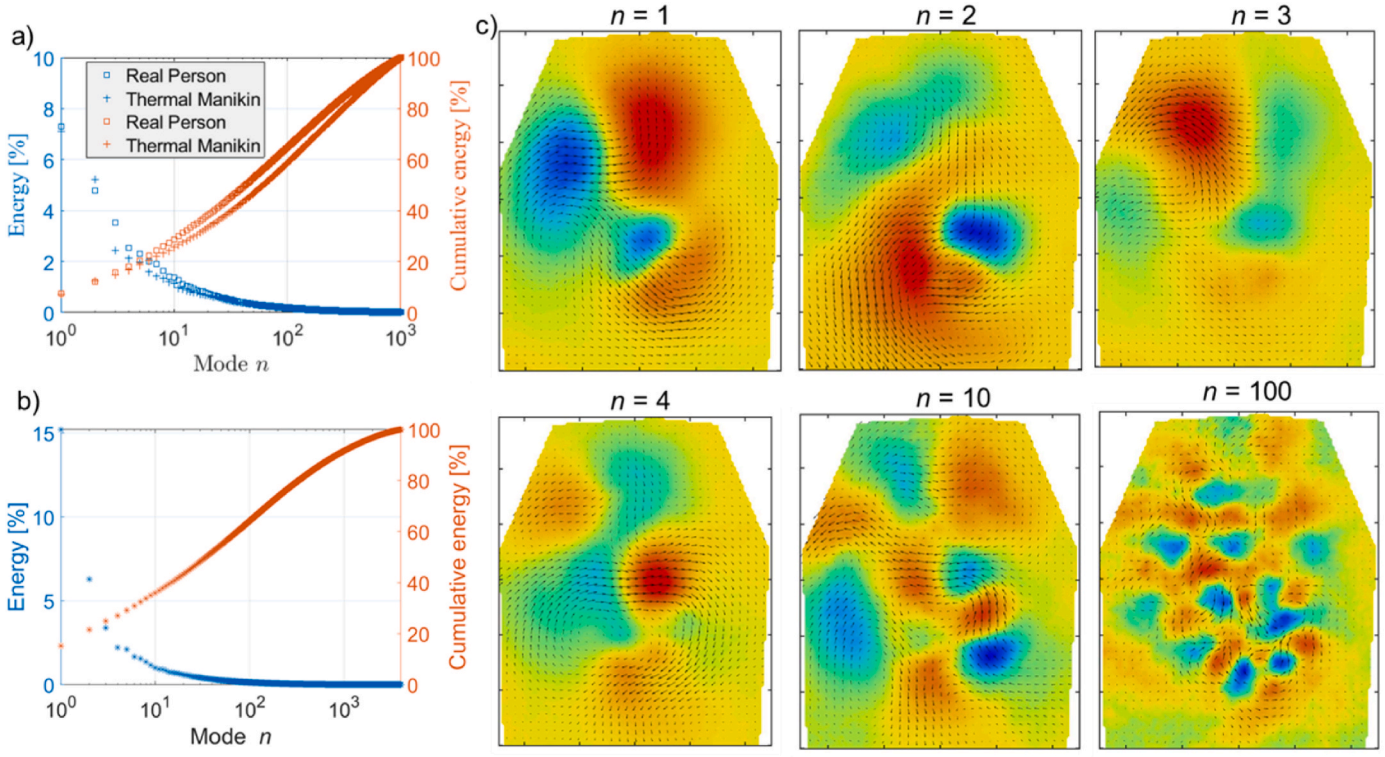

Fig. 8. Energy distributions of POD modes: (a) comparison of the thermal manikin and real person, (b) with ensemble of the snapshots from cases: thermal manikin, real person normal breathing, with mask and talking. (c) The POD spatial modes with the ensemble case as in (b). Here the in-plane velocity is represented by vectors, and the color contours indicate the vertical velocity (normalized with the peak of the mode). The x and y scales of the contour are the same as in Fig. 7. (For interpretation of the references to color in this figure legend, the reader is referred to the Web version of this article.)

cases, revealing the scales and shapes of the fluctuations. Primary modes illustrate the large-scale meandering of the thermal plume. For instance, mode 1 displays the frontal lobe deflection, nearly rotating around the center of the head. Additionally, the plume directly over the head also displaces slightly. Higher modes indicate progressively smaller scales as observed for $n = 10$ and 100 (cf. Fig. 8c). Still these scales remain comparable to the size of the macroscopic field of view and hence the decrease in energy of modes is gradual (cf. Fig. 8b).

The distribution observed here is similar to the cases of buoyant jets and thermal plumes from cooking presented in literature [30,31]. A study on the thermal plume from a manikin found in literature [20] with POD analysis revealed that first four modes contained more than 50% of the total energy. However, it needs to be emphasized that the case in Ref. [20] is a thermal manikin in confined space and that the area considered for POD analysis is small. An additional POD analysis on the 2D PIV data (data shown in supplementary information) obtained here with a smaller window revealed that the energy to be contained in fewer modes and approaching that of found in Ref. [20]. This suggests that the entire fluctuations of the thermal plume, particularly related to the frontal lobe, are not captured in the 2D PIV visualization.

4.3. Integral properties

Integral fluxes like volumetric flux V, momentum flux I, buoyancy force density P, and enthalpy flux Q are determined by [16,32].

$$V = \sum w \cdot \Delta A \tag{2}$$

$$I = \rho \sum w^2 \cdot \Delta A \tag{3}$$

$$P = \rho g \beta \sum \Delta T \cdot \Delta A \tag{4}$$

$$Q = \rho C_p \sum (\Delta T w) \cdot \Delta A \tag{5}$$

where ρ is the density of air (here taken as 1.2 kg/m^3), and w is the z-component of the velocity, ΔA is the cell size, g is the acceleration due to gravity, β is the coefficient of thermal expansion of air (here taken as 0.0034 1/K), ΔT is the excess temperature, and C_p is the heat capacity of air (here taken as 1 kJ/(kg K)).

The determined fluxes from the experimental data with the thermal manikin and various cases with the real person are presented in Fig. 9. It is observed that the volumetric flux and momentum flux quantities are similar in all cases for the real person. In comparison, the volumetric flux of the manikin is slightly lower than that of the real person. The momentum flux is similar in case of the thermal manikin and the real person.

For the calculation of the buoyancy force density and the enthalpy flux, one needs the measurement of the temperature field in a plane above the head. This was conducted in an independent trial with the thermal manikin. A total area of 720 mm × 720 mm in the horizontal plane above the head of the manikin was scanned with three PT100 temperature sensors connected on a x-y traverse system with a sensor spacing of 40 mm. The tips of the sensors were located at the same height as the velocity measurement plane (0.3 m above the head). From the measured temperatures, the temperature increase (ΔT) was calculated with respect to the room temperature, which was captured by the reference sensor at the same time instances, see Fig. 1b. This approach takes into account the increasing temperature in the room due to the power input from the manikin. The measured temperature excess above the thermal manikin is presented in Fig. 10. Similar to the velocity measurements, the peak temperature excess is off centered. Further, the lateral extent of the temperature excess is less compared to the w-velocity component.

The derived integral buoyancy force density and enthalpy flux are $P = 0.0042 \pm 0.0003$ kg/s^2 and $Q = 15.5 \pm 1.4$ W, respectively (where the confidence interval is one standard deviation). Since the temperature distribution is measured over a long time span, the measurements are an average of the plume meandering and need to be considered as an approximate. For a similar case of a thermal manikin (72 W) with no breathing reported in literature [15], the derived values are $P = 0.0042$ kg/s^2; $Q = 16.5$ W at 0.7 m above the manikin.

It is instructive to compare the measured enthalpy flux to the total power input to the thermal manikin. It is interesting to note that the total

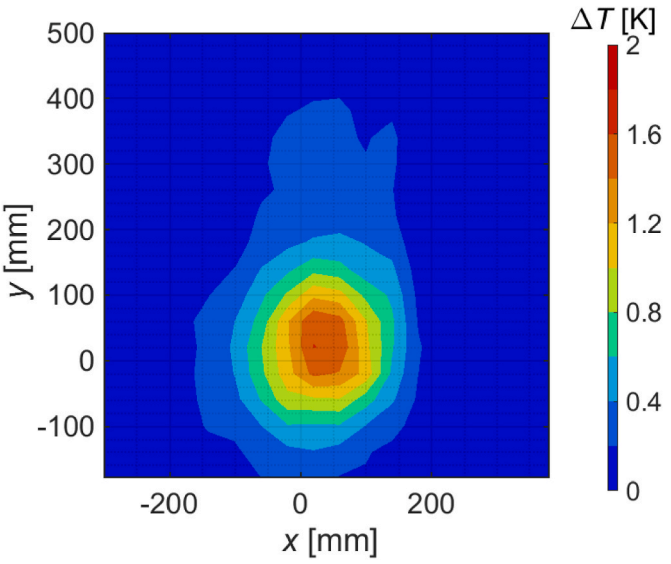

Fig. 10. Temperature excess map above the thermal manikin. $x = 0$, $y = 0$ is directly above the center of the head. The room temperature is measured at the location shown in Fig. 1b.

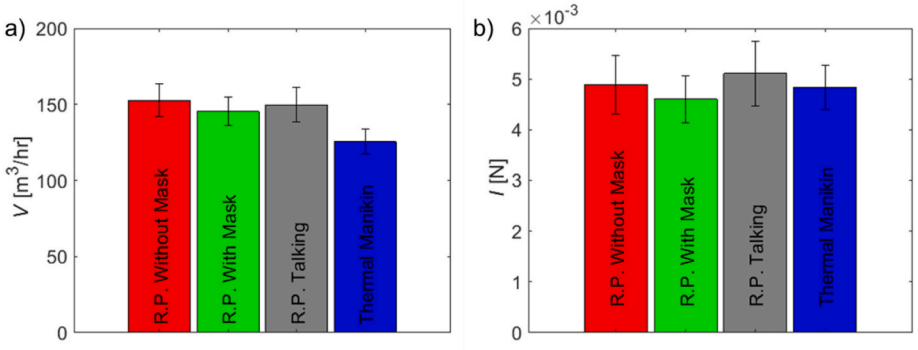

Fig. 9. Comparison of the integral fluxes between the real person and the thermal manikin: (a) volumetric flux, and (b) momentum flux.

power input to the manikin is 80 W. However, the measured enthalpy flux carried by the thermal plume at 0.3 m above the head is only a fraction of it (~20%).

The total convective heat input from the manikin would be the measured one above the head in case there is no vertical temperature gradient in the room. However, this is not the case when there is a vertical temperature gradient in the room as the plume continuously entrains air from the room. Hence, in case of the energy conservation analysis, the manikin heats the air at the botom near its foot with base temperature of the room and further adds heat from the room through the entrainment as it rises. Since the enthalpy flux calculated above is with respect to the room temperature at the measured height (0.3 m above head), the measured value is lower than the total convective heat input to the room from the manikin. Another extreme for the total convective heat input can be approximated by considering the base temperature of the room. In this approximation, the heat input due to entrainment is neglected, as the entrained air is at higher temperature (due to room vertical temperature gradient) compared to the base temperature. Table 2 lists the enthalpy flux considering the room base temperature for different vertical temperature gradient in the room.

In reality, the enthalpy flux is expected to be in-between that of calculated with the vertical temperature gradient in the room (say 0.34 K/m) and the one calculated with respect to the room temperature at 0.3 m above head. In order to calculate the exact contribution, one needs to know the entrainment volume as a function of the height of the thermal manikin.

An approximation for the heat transfer contribution between the manikin and the room might also be calculated by considering the electrical analogy. For the real human, the mechanisms of heat transfer involved are: convection, radiation, respiration and evaporation [33]. For the thermal manikin case, only convection and radiation heat transfer must be considered. In a simplified one-dimensional approximation, the radiative and convective resistances can be written as:

$$R_{rad} = \frac{1}{\varepsilon\sigma A F_{12}\left(T_s^2 + T_{room}^2\right)\left(T_s + T_{room}\right)};\ R_{conv} = 1 \Big/ \left(h_c A\right) \tag{6}$$

ε is the emissivity of the body, σ is the Stefan's Boltzmann constant, A is the surface area of the body losing heat, F_{12} is the view factor, T_s is the temperature of the body losing heat, T_{room} is the average room temperature, and h_c is the convective heat transfer coefficient.

The effective resistance (R) in parallel is:

$$\frac{1}{R} = \frac{1}{R_{rad}} + \frac{1}{R_{conv}} \tag{7}$$

The total heat flow can be related to the temperature drop between the manikin surface and the room temperature as $Q = (T_s - T_{room})/R$. The resulting equation can be solved for T_s and then the relative contribution of the convective and radiative heat transfer is found. Here, we assume a view factor of 1 between the manikin and the room, an emissivity of manikin = 0.9, and the surface area of the thermal manikin of 1.9 m^2. For an average room temperature of 25 °C Table 3 lists the calculated values for the total power of 80 W. An approximation of the convective heat transfer coefficient is found to be ~2.5 W/(m^2K) by considering a 1 m vertical plate heat transfer [27]. In general, the convective heat transfer of the human body is dependent on the posture of the body, the room temperature and the room conditions [34]. For natural convection in sitting position, the value varies between 2.2 and 3.5 depending on the correlation and the surface temperature of the thermal manikin [34]. Here, the measured temperature of the thermal manikin is 5–6 °C above the room temperature (25 °C).

Table 2
Calculated enthalpy flux considering the vertical temperature gradient dT/dz in the room.

dT/dz [K/m]	Q [W]	Q [in % of total power]
0	15.45	19.3
0.20	25.89	32.4
0.25	28.50	35.6
0.30	31.11	38.9
0.35	33.73	42.2

Table 3
The surface temperature, the radiation heat transfer, and the convective heat transfer by the effective resistance calculation.

Convective heat transfer coefficient h [W/(m^2K)]	T_s [°C]	Q_{rad} [W]	Q_{conv} [W]
2.2	30.43	57.29	22.71
2.5	30.23	55.14	24.86
2.8	30.05	53.14	26.86
3.0	29.93	51.89	28.11
3.2	29.82	50.69	29.31
3.5	29.66	48.99	31.01

The resulting surface temperature (T_s) as well as the radiative (Q_{rad}) and convective heat transfer (Q_{conv}) are listed in Table 3.

It is observed that the radiation heat transfer to the room dominates compared to the convection. It is interesting to note that the prior numerical simulation [33] also revealed that radiation is the major contribution for heat transfer to the room.

4.4. Simulation results

The comparison of the locally resolved volume flows of the two integration types of the heat loads (see Fig. 4) at a height of 1.6 m is shown in Fig. 11. The volumetric flow due to a central heat load influences the neighboring zones beside the dummy. If all positive values are added up (zones (x_y) 4_3, 5_2, 5_3, 5_4, 6_2, 6_3 and 6_4), this results in a total volume flow of 154 m^3/h. If the heat load is introduced into the model proportionally over several zones, more air rises over the legs and less over the center of the body (chest and head). This results in a lower total volume flow of 135 m^3/h. Due to the higher temperature with the central heat load, a larger buoyancy volume flow is formed than with the separated heat load. Here, a higher proportion flows to the side and not upwards.

If the simulation values are compared with the measured buoyancy flows, a good correspondence of both can be noticed (see Fig. 12). The simulated values lie between the measured values of the real person and the thermal manikin. In addition, the deviation of the simulation volume flows due to the different integration of the heat loads corresponds approximately the deviation of the measured buoyancy flow between the dummy and a real person.

The total buoyancy volume flow for the finer model is 160.7 m^3/h, which is slightly higher than for the original models. Since the buoyancy volume flow is considered at a height of 1.6 m, the value is mainly dependent on the heat release in the upper area in the immediate vicinity. The head and shoulder area emits 3 W more here and includes 8 zones instead of one. This leads to the increased buoyancy volume flow. The detailed results of this model are provided in Supplementary Information (8.2).

The excess temperatures in the test room are shown in Fig. 13. A maximum temperature excess of 0.6 K directly above the head is simulated. Further away from the heating load, no excess temperature can be detected. The excess temperatures in the model with the finer grid also yield a maximum value of 0.6 m/s over the head. These values are lower than the measured temperature excess (see Fig. 10). This is explained by the zonal model approach. The simulated temperatures represent the mean values of a zone and not absolute values. Thus, finely resolved peak values cannot be represented.

If the enthalpy flux is calculated from the simulated volume flows and temperature excesses (see equation (5) and Figs. 11 and 13), it results in a flux of 16.9 W (central heat load), 18.0 W (proportionate heat load), and also 16.9 W for the finer grid model. This includes enthalpy

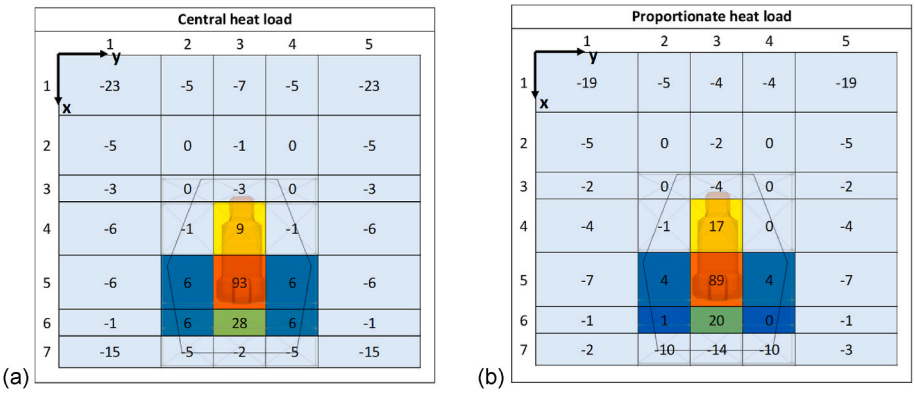

Fig. 11. Sectional views at the height of the viewing plane (1.6 m) with simulated vertical buoyancy volume flows in m^3/h (upward flow: positive values) by (a) a central and (b) a proportional implementation of the heat load.

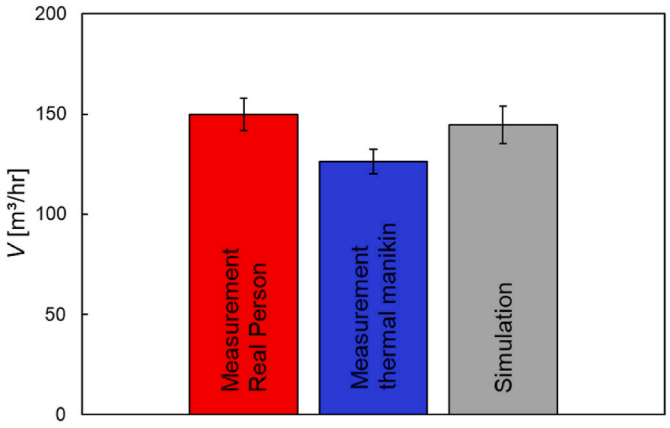

Fig. 12. Comparison of buoyancy volumetric fluxes between measurement and simulation.

flux upward, but not to the side. The simulation model can also be used to calculate the proportions of heat dissipation by radiation and convection. The calculations are the based on the following equations:

$$Q_{conv} = h_c(T_s - T_{air})A \tag{6}$$

$$Q_{rad} = \sigma\varepsilon\left(T_s^4 - T_{air}^4\right)A \tag{7}$$

The air temperature T_{air} is equal to the room temperature in both equations. The convective heat transfer coefficient h_c acts as an input parameter and is set to 3.5 W/(m^2K). The results are listed in Table 4.

Comparing these values with the calculated data in Table 3, a good agreement can be observed.

To analyze how convective heat is distributed, a virtual box is created around the human and the enthalpy fluxes are balanced over the respective boundary surfaces. The result from the simulation with a proportional implementation of the heat load is visualized in Fig. 14.

5. Conclusion

The results presented here show that the thermal plume from a manikin without breathing function has many similarities in the average flow field above the head with the field induced by a real person. The vertical velocity component reaches a peak of 0.17 m/s for the real person, which is lower than the peak of 0.23 m/s observed for the thermal manikin. However, the structures of the thermal plumes

Table 4
Contribution of the radiation heat transfer, convective heat transfer and surface temperature by the simulation model.

	Convective heat transfer coefficient h_c [W/(m^2K)]	T_s [°C]	Q_{rad} [W]	Q_{conv} [W]
Central heat load	3.5	29.2	51.1	28.9
Proportional heat load			50.6	29.4
Zone 4_3_1	3.5	27.6	4.3	3.0
Zone 4_3_2		27.9	5.0	3.7
Zone 5_3_2		29.5	25.7	14.3
Zone 5_3_3		29.9	15.6	8.4
Proportional heat load (finer grid)	3.5		50.6	29.6

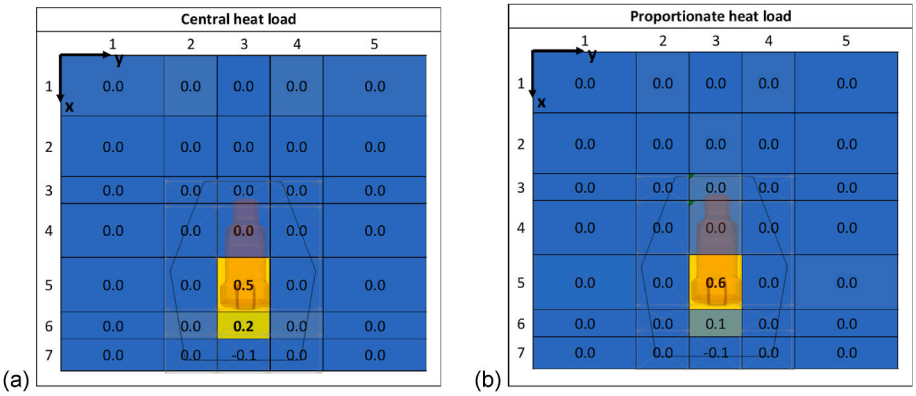

Fig. 13. Sectional views at the height of the viewing plane (1.6 m) with temperatures exceeding the room temperature (zone 2_1) by (a) a central and (b) a proportional implementation of the heat load.

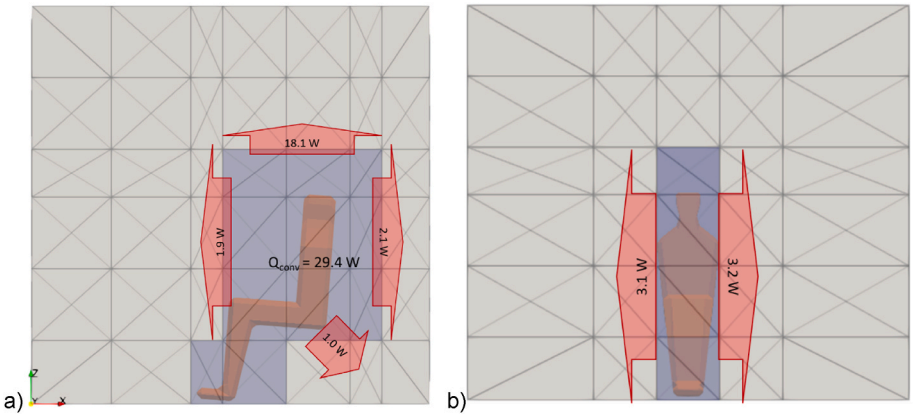

Fig. 14. Sectional views of the distribution of convective heat influx by a person in (a) *x*-*z* plane and (b) *y*-*z*-plane.

resemble to some extent in both cases, revealing bi-lobe like structure with the secondary lobe to the front. The second lobe in case of thermal manikin is possibly due to the thermal plume from the legs. The study found that the thermal plume from the real person had an average volume flux of 153 m^3/hr, while the thermal manikin exhibited 125 m^3/hr. Momentum flux was consistent at 0.005 N for both cases. Furthermore, the breathing, speaking, and with mask cases of the real person resulted in similar integral fluxes with changes in the nature of the extent of the plume. The characterizations of these phenomena are important because they cannot be simulated by the manikin, while they affect the extent and strength of the thermal convection flow. The fluctuating flow field also revealed similarities between the real person and the thermal manikin including the energy distribution in different modes by POD analysis. This indicates that the thermal manikin reasonably simulates the major flow characteristics and the fluctuating flow observed in the real person thermal plume. Further, considering few modes of the flow is insufficient to capture the flow field established by the manikin/human. Enthalpy flux calculation showed that the radiation mechanism dominates in the scenarios discussed.

In summary, upward rising flow from a human at regular scenarios of a sitting person (no activity) has been characterized and compared with a thermal manikin. This study has highlighted the necessity of large field of view PIV to completely capture the flow dynamics of the human thermal plume. The heat interaction of the human/manikin with the surroundings is dominated by radiation; however, the convective flow induced is significant and important for indoor ventilation design. Furthermore, it can be implemented in a zonal model with a good correspondence between simulated and measured data.

CRediT authorship contribution statement

Abhilash Sankaran: Writing – review & editing, Writing – original draft, Visualization, Methodology, Investigation, Formal analysis, Data curation. **Rainer Hain:** Writing – review & editing, Resources, Methodology. **Christina Matheis:** Writing – original draft, Software, Investigation, Data curation. **Thomas Fuchs:** Writing – review & editing, Visualization, Methodology. **Victor Norrefeldt:** Software, Methodology. **Gunnar Grün:** Funding acquisition, Conceptualization. **Christian J. Kähler:** Supervision, Funding acquisition, Conceptualization.

Declaration of competing interest

The authors declare that they have no known competing financial interests or personal relationships that could have appeared to influence the work reported in this paper.

Data availability

Data will be made available on request.

Acknowledgement

The authors acknowledge funding by “Die Beauftragte der Bundesregierung für Kultur und Medien (BKM)” through the “CineCov” project and “dtec.bw – Digitalization and Technology Research Center of the Bundeswehr through project LUKAS”. dtec.bw is funded by the European Union – NextGenerationEU.

Appendix A. Supplementary data

Supplementary data to this article can be found online at https://doi.org/10.1016/j.buildenv.2024.111290.

References

[1] D. Licina, J. Pantelic, A. Melikov, C. Sekhar, K.W. Tham, Experimental investigation of the human convective boundary layer in a quiescent indoor environment, Build. Environ. 75 (2014) 79–91.
[2] R. Yang, C.S. Ng, K.L. Chong, R. Verzicco, D. Lohse, Do increased flow rates in displacement ventilation always lead to better results? J. Fluid Mech. 932 (2022). A3 1-12.
[3] J. Ma, H. Qian, P.V. Nielsen, L. Liu, Y. Li, X. Zheng, What dominates personal exposure? Ambient airflow pattern or local human thermal plume, Build. Environ. 196 (2021) 107790.
[4] D. Licina, A. Melikov, C. Sekhar, K.W. Tham, Human convective boundary layer and its interaction with room ventilation flow, Indoor Air 25 (2015) 21–35.
[5] R.K. Bhagat, M.D. Wykes, S.B. Dalziel, P.F. Linden, Effects of ventilation on the indoor spread of COVID-19, J. Fluid Mech. 903 (2020). F1 1-18.
[6] J. Ma, H. Qian, F. Liu, X. Zheng, Performance analysis of a novel personalized air curtain for preventing inhalation of particulate matters in industrial environments, J. Build. Eng. 58 (2022) 105014.
[7] S. Sun, J. Li, J. Han, How human thermal plume influences near-human transport of respiratory droplets and airborne particles: a review, Environ. Chem. Lett. 19 (2021) 1971–1982.
[8] J. Zong, J. Liu, Z. Ai, M.K. Kim, A review of human thermal plume and its influence on the inhalation exposure to particulate matter, Indoor Built Environ. 31 (2022) 1758–1774.
[9] Y. Yan, X. Li, J. Tu, Thermal effect of human body on cough droplets evaporation and dispersion in an enclosed space, Build. Environ. 148 (2019) 96–106.
[10] B.A. Craven, G.S. Settles, A computational and experimental investigation of the human thermal plume, J. Fluid Eng. 128 (2006) 1251–1258.
[11] X. Tang, P.K. Misztal, W.W. Nazaroff, A.H. Goldstein, Volatile organic compound emissions from humans indoors, Environ. Sci. Technol. 50 (2016) 12686–12694.
[12] G.S. Settles, H.A. Gowadia, S.B. Strine, T.E. Johnson, W.H. Makky, The natural aerodynamic sampling of trace explosives from the human body, in: Proceedings of the 2nd FAA Conference on the Aviation Security Problem and Related Technologies, SPIE CR42, Atlantic City, NJ, 1996, November, pp. 65–70.
[13] B. Koelblen, A. Bogdan, Impact of clothing, breathing and body posture on the shaping of a thermal plume above a human, Int. J. Vent. 13 (2015) 397–410.
[14] D. Zukowska, A. Melikov, Z. Popiolek, Impact of personal factors and furniture arrangement on the thermal plume above a sitting occupant, Build. Environ. 49 (2012) 104–116.

[15] D. Zukowska, A. Melikov, Z. Popiolek, J. Spletsteser, Impact of breathing on the thermal plume above a human body, in: Proceedings of the 12th International Conference on Air Distribution in Rooms–Roomvent, 2011, June. Trondheim, Norway.
[16] A. Bogdan, K. Ogłodziński, M. Szyłak-Szydłowski, Analysis of thermal plumes forming over male human subjects, J. Build. Eng. 45 (2022) 103596.
[17] A.K. Melikov, Z. Popiolek, M.C.G. Silva, I. Care, T. Sefker, Accuracy limitations for low-velocity measurements and draft assessment in rooms, HVAC R Res. 13 (2007) 971–986.
[18] X. Cao, J. Liu, N. Jiang, Q. Chen, Particle image velocimetry measurement of indoor airflow field: a review of the technologies and applications, Energy Build. 69 (2014) 367–380.
[19] D. Marr, T. Khan, M. Glauser, H. Higuchi, J. Zhang, On particle image velocimetry (PIV) measurements in the breathing zone of a thermal breathing manikin, Build. Eng. 111 (2005) 299–305.
[20] J. Li, J. Liu, J. Pei, K. Mohanarangam, W. Yang, Experimental study of human thermal plumes in a small space via large-scale TR PIV system, Int. J. Heat Mass Tran. 127 (2018) 970–980.
[21] C. Inard, H. Bouia, P. Dalicieux, Prediction of air temperature distribution in buildings with a zonal model, Energy Build. 24 (1996) 125–132.
[22] V. Norrefeldt, G. Grün, K. Sedlbauer, Vepzo – velocity propagating zonal model for the estimation of the airflow pattern and temperature distribution in a confined space, Build. Environ. 48 (2012) 183–194, https://doi.org/10.1016/j.buildenv.2011.09.007.
[23] A. Parikh, T. Fuchs, M. Bross, C.J. Kähler, LEGO calibration targets for large-FOV particle image velocimetry, Exp. Fluid 64 (2) (2023) 34.
[24] J. Voss, Revisiting Office Space Standards, Haworth, Grand Rapids, MI, 2000, pp. 1–6.
[25] A. Schröder, D. Schanz, J. Bosbach, M. Novara, R. Geisler, J. Agocs, A. Kohl, Large-scale volumetric flow studies on transport of aerosol particles using a breathing human model with and without face protections, Phys. Fluids 34 (2022) 035133.
[26] M. Raffel, C.E. Willert, F. Scarano, C.H. Kähler, S.T. Wereley, J. Kompenhans, Particle Image Velocimetry: a Practical Guide (3rd Edition), Springer, Berlin, 2018.
[27] R. Karwa, Heat and Mass Transfer (2nd Edition), Springer, Singapore, 2020.
[28] LaVision, Product Manual DaVis 10.2 Software, LaVision GmbH, Göttingen, 2021.
[29] Modelica Association, Modelica, https://modelica.org/, accessed 31. November 2022..
[30] W. Chen, J. Liu, J. Li, X. Dai, P. Wang, C. Wang, Assessment of a confined thermal plume by PIV combined with POD analysis, Appl. Therm. Eng. 188 (2021) 116590.
[31] R. Watanabe, T. Gono, T. Yamagata, N. Fujisawa, Three-dimensional flow structure in highly buoyant jet by scanning stereo PIV combined with POD analysis, Int. J. Heat Fluid Flow 52 (2015) 98–110.
[32] S. Mierzwinski, Air Motion and Temperature Distribution above a Human Body in Result of Natural Convection, vol. 45, Royal Institute of Technology, Stockholm, Sweden, 1981.
[33] S. Murakami, S. Kato, J. Zeng, Combined simulation of airflow, radiation and moisture transport for heat release from a human body, Build. Environ. 35 (2000) 489–500.
[34] A.V.M. Oliveira, A.R. Gaspar, S.C. Francisco, D.A. Quintela, Analysis of natural and forced convection heat losses from a thermal manikin: comparative assessment of the static and dynamic postures, J. Wind Eng. Ind. Aerod. 132 (2014) 66–76.